Physics of Plasmas ARTICLE scitation.org/journal/php

Multi-fluid and kinetic models of partially ionized magnetic reconnection

Cite as: Phys. Plasmas **28**, 042108 (2021); doi: 10.1063/5.0039860
Submitted: 7 December 2020 · Accepted: 5 March 2021 ·
Published Online: 13 April 2021

View Online Export Citation CrossMark

J. Jara-Almonte,[1,a)] N. A. Murphy,[2] and H. Ji[1]

AFFILIATIONS

[1]Princeton Plasma Physics Laboratory, Princeton, New Jersey 08543, USA
[2]Center for Astrophysics, Harvard and Smithsonian, Cambridge, Massachusetts 02138, USA

[a)]Author to whom correspondence should be addressed: jjaraalm@pppl.gov

ABSTRACT

Magnetic reconnection in partially ionized plasmas is a ubiquitous and important phenomenon in both laboratory and astrophysical systems. Here, simulations of partially ionized magnetic reconnection with well-matched initial conditions are performed using both multi-fluid and fully-kinetic approaches. Despite similar initial conditions, the time-dependent evolution differs between the two models. In multi-fluid models, the reconnection rate locally obeys either a decoupled Sweet–Parker scaling, where neutrals are unimportant, or a fully coupled Sweet–Parker scaling, where neutrals and ions are strongly coupled, depending on the resistivity. In contrast, kinetic models show a faster reconnection rate that is proportional to the fully-coupled, bulk Alfvén speed, $v_A^\star$. These differences are interpreted as the result of operating in different collisional regimes. Multi-fluid simulations are found to maintain $\nu_{ni}L/v_A^\star \gtrsim 1$, where ν_{ni} is the neutral–ion collision frequency and L is the time-dependent current sheet half-length. This strongly couples neutrals to the reconnection outflow, while kinetic simulations evolve to allow $\nu_{ni}L/v_A^\star < 1$, decoupling neutrals from the reconnection outflow. Differences in the way reconnection is triggered may explain these discrepancies.

I. INTRODUCTION

Magnetic reconnection is the breaking and rejoining of magnetic field lines in a highly conducting plasma.[1–4] This fundamental plasma process transforms magnetic energy into the kinetic energy of bulk flows, plasma heating, and particle acceleration. Reconnection occurs ubiquitously in magnetized heliophysical, laboratory, and astrophysical plasmas.

Historically, most studies on reconnection have investigated fully ionized plasmas.[1–3] However, reconnection is also an important process in partially ionized plasmas in nature and the laboratory.[4] Reconnection in the partially ionized low solar atmosphere is associated with chromospheric jets,[5,6] Ellerman bombs,[7,8] and UV bursts.[8,9] Reconnection may also play an important role in astrophysical systems, such as the interstellar medium, molecular clouds, or protoplanetary disks.[4,10]

In weakly ionized plasmas, the majority of the mass density resides in a neutral species, e.g., atomic hydrogen or helium on the Sun. This neutral species is collisionally coupled to the ionized component thorough a complex variety of collisional processes including elastic scattering, charge exchange, excitation/de-excitation, and ionization and recombination. In general, these processes have both non-trivial species and energy dependencies, which significantly complicate the underlying physics involved.

To simulate partially ionized plasmas, a hierarchy of models has been used, including single-fluid, multi-fluid, and kinetic approaches. In the simplest single fluid models, all species, neutrals, ions, and electrons, are assumed to be well-coupled via collisions so that only a single bulk-fluid momentum equation is required. This is equivalent to the low-frequency assumption, $\omega \ll \nu_{ni}$, where ν_{ni} is the neutral–ion collision frequency. For collisional reconnection, the characteristic frequency is $\omega \sim v_A^\star/L$ where $v_A^\star \equiv B/\sqrt{\mu_0(m_i n_i + m_n n_n)}$ and L is the current-sheet half-length. The single-fluid equations can be further simplified by neglecting plasma pressure, $\beta \equiv 4\mu_0 nkT/B^2 = 0$, which leads to the well-known ambipolar diffusion term in the generalized Ohm's law.[11,12] However, when these assumptions are violated, a more complete model must be used.

The multi-fluid approach divides the system into two or more separate, interacting fluids. In the most general case, this would include an individual fluid for each component. In the HiFi computational modeling framework,[13–15] a two-fluid model consisting of a neutral fluid and a Hall MHD plasma fluid has been extensively used to study reconnection in the chromosphere.[16–21] The

advantage of multi-fluid models is that the plasma and neutral fluid are allowed to decouple at small spatial scales and at high frequencies. HiFi simulations have demonstrated that decoupling between the neutral and charged components plays an important role in reconnection.[16]

Finally, the kinetic approach self-consistently evolves the particle distribution function for each species. Particle-in-cell (PIC) techniques are an efficient approach to kinetic simulations and are highly suited for modeling collisionless or weakly collisional plasmas. Kinetic approaches are able to accurately model transport coefficients (e.g., resistivity, viscosity, or heat flux) at all scales, including below the mean-free-path where fluid models are invalid. Recent PIC simulations have demonstrated that the transition from collisional to collisionless reconnection in partially ionized plasmas occurs at smaller scales than previously predicted.[22]

Each of these methodologies has advantages and disadvantages, but to date, there has been no direct comparison between these different approaches despite inconsistent results in the literature. In particular, the questions such as when fast reconnection occurs and what the peak reconnection rate is are not well understood. Experiments[23] and PIC simulations[22] have concluded that the reconnection rate scales as $\chi^{1/2}$, where $\chi \equiv n_i/(n_i + n_n)$ is the ionization fraction, and occurs on scales smaller than the ion inertial length $d_i = c/\omega_{pi}$. In contrast, analytic three-fluid results predicted an ionization-fraction independent reconnection rate at scales smaller than the bulk inertial length $d^\star \equiv d_i\chi^{-1/2}$.[24] Previous multi-fluid simulations have not reported fast, Hall-mediated reconnection and suggested that if it does occur, it is on scales smaller than $d^\star$.[18,19]

Here, a direct comparison and benchmark between multi-fluid and PIC simulations of partially ionized reconnection is performed. The reconnection rate is found to be faster in PIC simulations, especially for moderately ionized cases with $\chi \gtrsim 0.1$. The reconnection rate in multi-fluid simulations is shown to obey either a fully coupled or decoupled Sweet–Parker scaling depending on the resistivity used; whereas in kinetic simulations, the rate is proportional to the bulk Alfvén speed. However, in all cases the sheet aspect ratio is observed to follow a local, fully-coupled Sweet–Parker scaling. This effect is not well understood, but suggests that neutrals play an important role in determining the current sheet structure even on small scales. Overall, it is suggested that the differences between models are the result of operating in different collisionality regimes; multi-fluid simulations evolve to maintain $\nu_{ni}L/v_A^\star \gtrsim 1$, where ions and neutrals are coupled in the outflow, while some kinetic simulations, and previous laboratory experiments,[23] may have $\nu_{ni}L/v_A^\star < 1$, where ions and neutrals are decoupled in the outflow.

II. NUMERICAL METHODS

In this paper, numerical simulations of magnetic reconnection in partially ionized plasmas are performed using both fully kinetic PIC and multi-fluid techniques. These two approaches are fundamentally different. By directly comparing the simulation results, the relative importance of kinetic effects on plasma transport and reconnection can be more clearly understood. This section contains a summary of the problem setup as well as the numerical methods and techniques used in each set of simulations.

A. Problem setup

To study the fundamental microphysics associated with partially ionized reconnection, a prototypical Harris sheet geometry is used in a Cartesian coordinate system, $(\hat{\mathbf{x}}, \hat{\mathbf{y}}, \hat{\mathbf{z}})$, where $\hat{\mathbf{x}}$ is the inflow direction, $\hat{\mathbf{y}}$ is the out-of-plane direction, and $\hat{\mathbf{z}}$ is the outflow direction. The initial magnetic field varies as

$$\vec{B} = B_0 \tanh\left(\frac{x}{\delta}\right)\hat{\mathbf{z}} \tag{1}$$

and the plasma density as

$$n_i = n_e = n_b + n_0\,\mathrm{sech}^2\left(\frac{x}{\delta}\right). \tag{2}$$

Neutrals are included by imposing a uniform and stationary background with number density $n_n = n_b(1-\chi)/\chi$, where $\chi \equiv n_i/(n_n + n_i)$ is the ionization fraction. All species are initialized with a uniform temperature $k_BT = 2.5$ eV. The background density is chosen such that $\beta_0 = 2\mu_0 n_b T/B_0^2 = 0.3$. These initial conditions satisfy neither force balance (due to ion–neutral and Coulomb friction) nor ionization balance. However, force balance is quickly realized within a collisional relaxation time ($\nu_{in,0}^{-1} \sim \Omega_{i0}^{-1} \equiv eB_0/m_ic$ for the parameters chosen). In this manuscript, inelastic processes, including ionization and recombination, are neglected to be consistent with previous theoretical studies.[22,24] The neutral and ion species are assumed to be ${}^4_2\mathrm{He}^{0+}$ and ${}^4_2\mathrm{He}^{1+}$, respectively.

With the exception of one kinetic case (described below), all simulations in this manuscript used a domain size of $L_x = 200d_{i0}$ by $L_z = 400d_{i0}$ where $d_{i0} = c/\omega_{pi0}$ is the ion inertial length defined using n_0. Periodic boundary conditions are used in $\hat{\mathbf{z}}$ and perfectly conducting and reflecting boundary conditions in $\hat{\mathbf{x}}$. The initial current sheet thickness was taken to be $\delta_0 = 1d_{i0}$ for kinetic simulations, $\delta_0 = 4d_{i0}$ for the matched multi-fluid simulations, and $\delta_0 = 8d_{i0}$ for the multi-fluid simulations with higher resistivity.

Previously, it was observed that the kinetic reconnection rate was system size dependent at low ionization fraction.[22] To test the sensitivity of a reference case, $\chi_0 = 0.1$, to both system size and initial current sheet thickness, an additional kinetic simulation was performed with $L_z = 800d_{i0}$ and $\delta_0 = 2d_{i0}$ (all other parameters are the same). This case is denoted by $\star$ in Figs. 4–6. There is negligible difference with the $L_z = 400d_{i0}$ cases, suggesting that the simulations in this manuscript are not sensitive to δ_0 or system size, at least for $\chi_0 \geq 0.1$.

All kinetic simulations in this manuscript use reduced parameters $m_i/m_e = 40$ (with $m_n = m_i + m_e$) and $\omega_{pe0}/\Omega_{e0} = 2$ ($c/v_{the0} = 4$) in order to reduce the computational cost. The grid size is 3162×6250 for the $L_z = 400d_{i0}$ cases and $3162 \times 12\,288$ for the $L_z = 800d_{i0}$ case. An average of 1000 particles per species per cell are used ($\sim 6 \times 10^{10}$ total particles for $L_z = 400d_{i0}$). A uniform, Courant–Friedrichs–Lewy (CFL)-limited, time step is used and is equal to $0.279\omega_{pe}^{-1}$ for the $L_z = 400d_{i0}$ cases. Collisions are performed every five time steps. Finally, to seed single X-line reconnection, a long wavelength perturbation is applied and described by the vector potential $\delta A_y = 0.004B_0L_z\cos(\pi x/L_x)\cos(2\pi z/L_z)$.

The multi-fluid simulations performed with HiFi had a resolution of 64 spectral elements along the outflow direction and 32 spectral elements along the inflow direction. The spectral element basis functions were eighth order for the matched simulations, and sixth

order for the higher resistivity simulations. Static mesh packing was used to concentrate resolution around the region of the current sheet. As a consequence, there were several spectral elements across the current sheet along the inflow direction even for the thinnest current sheets obtained.

As shall be described below, the manner in which collisional and dissipative processes are included in PIC and fluid simulations is fundamentally different. In order to match the two methods as closely as possible, the effective transport coefficients are approximated from the initial Maxwellian distribution functions in the PIC simulations and then used within the fluid simulations.

B. Kinetic simulations

Kinetic simulations are performed using the VPIC (vector particle-in-cell) PIC code.[25] VPIC is a fully explicit, electromagnetic PIC code that evolves the single-particle distribution function by integrating along the characteristics of the Vlasov equation. VPIC is highly optimized and has been previously used to study collisional reconnection in both fully ionized[26–28] and partially ionized[22] plasmas. Coulomb collisions are included using a standard particle-pairing algorithm.[26,29]

To include collisional processes between plasma species and neutrals, a Monte Carlo collision algorithm is used.[30] It is assumed that each collisional process may be written as a reaction of the form

$$n_A A + n_B B + \cdots \rightarrow n_X X + n_Y Y + \cdots, \tag{3}$$

where each reactant species (A, B, …) and each product (X, Y, …) species is modeled kinetically. Parameters for the HiFi simulations are given in SI units in Table I. At each collisional time step, the macroparticle list for each species is sorted by cell index, and, within each cell, the N_S macroparticles for each reactant species $S \in \{A, B, \ldots\}$ are identified. From these macroparticles, a random selection of

$$N = f \prod_S \binom{N_S + n_S - 1}{n_S} \tag{4}$$

sets of macroparticles are tested to potentially undergo reaction (3). This strategy allows generic reactions to occur, but in the case of simple binary collisions, $A + B \rightarrow \cdots$, then this is simplified as $N = f n_A n_B$. The sampling fraction, f, is chosen dynamically as described below. To see if a set of macroparticles $p = \{p_i\}$ with associated statistical weights $w = \{w_i\}$ collides, a uniform random number is tested against the probability of a collision

TABLE I. HiFi simulation parameters in physical units. These values were chosen to keep $\lambda_{in}/d_i = 0.5$ as based on a cross section for ion–neutral momentum transfer of 4×10^{-19} m^2. In all simulations, $k_B T = 2.5$ eV.

Case	χ	n_i (m^{-3})	B_{z0} (T)	L_z (m)	d_i (m)	η_0 ($\Omega \cdot$ m)
A1	0.3	2.21×10^{19}	1.22×10^{-2}	21.3	0.097	7.55×10^{-5}
A2	0.2	7.51×10^{18}	7.1×10^{-3}	36.4	0.17	1.29×10^{-4}
A3	0.1	1.48×18^{18}	31.6×10^{-3}	82	0.37	2.91×10^{-4}
A4	0.075	7.90×10^{17}	2.3×10^{-3}	112	0.51	3.99×10^{-4}
A5	0.05	3.33×10^{17}	1.5×10^{-3}	173	0.79	6.14×10^{-4}
A6	0.025	7.90×10^{16}	7.29×10^{-4}	355	1.6	1.26×10^{-3}
A7	0.01	1.23×10^{16}	2.87×10^{-4}	902	4.1	3.21×10^{-3}

$$P_{collide} = \frac{K(p)\, dt}{f\, dV \min(w)} \prod_i w_i, \tag{5}$$

where $K(p)$ is the reaction rate-constant for the set of macroparticles. If a collisional process is under-resolved, $P_{collide}$ may be greater than 1 for some sets. In this case, the sampling fraction is increased on the next collisional time step by $\max(P_{collide})$. If a collision is successful, each reactant macroparticle's momentum and/or statistical weight is updated with probability

$$P_{update}(p_i) = \frac{\min(w)}{w_i}. \tag{6}$$

This ensures that conservation properties of the underlying collision kinematics hold exactly for equal macroparticle statistical weights and in an average sense for unequal weights. Although unused in this work, ionization and recombination have been implemented, and for non-number preserving processes, product macroparticles are generated at the center-of-mass and with statistical weight $\min(w)$.

In general, the underlying kinematics depends on the type of collisional process. For non-relativistic, species-preserving, binary collisions, the momentum update for a particle of species $S = \{\alpha, \beta\}$ is given by

$$\mathbf{\Delta v} = \frac{2\delta^2}{1+\delta^2}\left[\mathbf{v_\beta} - \mathbf{v_\alpha} + \frac{|\mathbf{v_\alpha} - \mathbf{v_\beta}|}{\delta}\hat{\mathbf{v}}_\perp\right], \tag{7a}$$

$$\mathbf{v_S} = \gamma\left(\mathbf{v_S} \pm \frac{m_{\alpha\beta}}{m_S}\mathbf{\Delta v}\right) + (1-\gamma)\mathbf{v_{cm}}. \tag{7b}$$

Here, $m_{\alpha\beta} = m_\alpha m_\beta/(m_\alpha + m_\beta)$ is the reduced mass, $\mathbf{v_{cm}}$ is the center-of-mass velocity, $\hat{\mathbf{v}}_\perp$ is a randomly chosen unit vector orthogonal to $\mathbf{v}_\alpha - \mathbf{v}_\beta$, $\delta(E) = \tan\theta(E)/2$ where $\theta(E)$ is the scattering angle, $\gamma(E)$ is the coefficient of restitution, and $E = \frac{1}{2} m_{\alpha\beta}|\mathbf{v_\alpha} - \mathbf{v_\beta}|^2$ is the collision energy. For elastic collisions, $\gamma = 1$, and for inelastic collisions, the change in kinetic energy is $\Delta E = (\gamma^2 - 1)E$.

In this kinetic treatment, the differential scattering cross sections, $\partial\sigma/\partial\theta$, are prescribed rather than bulk fluid transport coefficients. To compute transport coefficients, moments of the Boltzmann collision integral must be evaluated for each process, but for sub-thermal drifts the coefficients depend only on the reduced transport cross sections

$$\sigma^{(n)}_{\alpha\beta}(E) = 2\pi \int_0^\pi \frac{\partial\sigma_{\alpha\beta}}{\partial\theta}(1 - \cos^n\theta)\sin\theta\, d\theta, \tag{8}$$

which describe the total ($n = 0$), momentum transfer ($n = 1$), and viscosity ($n = 2$) cross sections. For example, the collisional momentum transfer rate for non-drifting Maxwellian distributions is given by[31]

$$\nu_{\alpha\beta} = n_\beta v_{\alpha\beta} \frac{8}{3\sqrt{2\pi}} \frac{m_{\alpha\beta}}{m_\alpha} \int_0^\infty x^2 e^{-x} \sigma^{(1)}_{\alpha\beta}(x k_B T_{\alpha\beta})\, dx, \tag{9}$$

where $T_{\alpha\beta} = (m_\beta T_\alpha + m_\alpha T_\beta)/(m_\alpha + m_\beta)$ and $v_{\alpha\beta} = \sqrt{k_B T_{\alpha\beta}/m_{\alpha\beta}}$.

For the processes included, the included transport cross sections, along with $n = 1$ and $n = 2$ moments, are shown as function of collision energy in Fig. 1(a). For comparison with fluid models, these cross sections have been integrated over a thermal distribution to obtain the momentum transfer rates, $\nu_{\alpha\beta}$ which are shown in Fig. 1(b).

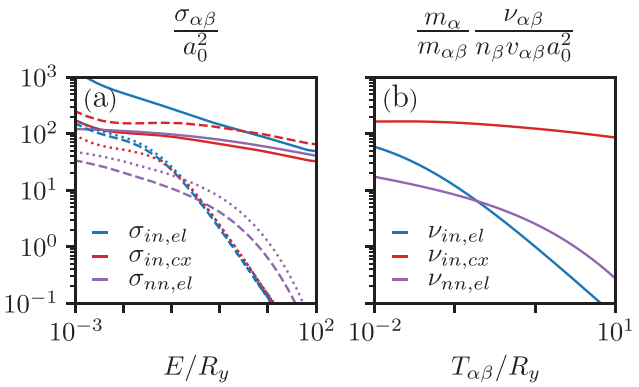

FIG. 1. Dimensionless cross sections and momentum transfer rates used in VPIC for ion–neutral elastic, $\{\sigma,\nu\}_{in,el}$, charge-exchange, $\{\sigma,\nu\}_{in,cx}$, and neutral–neutral elastic, $\{\sigma,\nu\}_{nn,el}$, scattering. (a) Lines show the total [$\sigma^{(0)}_{\alpha\beta}$, solid], momentum [$\sigma^{(1)}_{\alpha\beta}$, dashed], and viscosity [$\sigma^{(2)}_{\alpha\beta}$, dotted] integrated cross sections. (b) Momentum transfer rates obtained by integrating over non-drifting Maxwellian distributions according to Eq. (9).

Since reduced parameters (m_i/m_e and ω_{pe}/Ω_e) are used in PIC simulations, collisional cross sections must be scaled in order to maintain the same ratio between plasma and collisional scales (e.g., λ_{mfp}/d_i). For binary collisions, it is assumed that each cross section may be written as

$$\frac{\partial\sigma(E)}{\partial\theta} = a_0^2\frac{\partial\bar{\sigma}(E/R_y)}{\partial\theta}, \tag{10}$$

where E is the collision energy, a_0 is the Bohr radius, R_y the Rydberg energy ($\approx$13.6 eV), and $\partial\bar{\sigma}(x)/\partial\theta$ the dimensionless differential cross section. This normalization choice introduces two new dimensionless parameters, the fine structure constant, $\alpha = \sqrt{2R_y/m_ec^2} = \sqrt{2R_y/T_{e0}}(v_{the0}/c)$, and the linear density, $n_0a_0^2$. These constants are determined by the choices $T_{e0} = 2.5$ eV and $\lambda_{in}/d_{i0} = 0.5$, along with the typical value of $\sigma^{(1)}_{in,cx} \approx 150a_0^2 \approx 4\times10^{-19}$ m^2.

The methodology described above is general, and a complete set of collisional processes has been implemented within VPIC. However, in this manuscript only elastic processes are included in order to focus on the simplest case of partially ionized reconnection. Furthermore, electron–neutral collisions are neglected as the Coulomb collisional cross section is larger than the electron–neutral cross section across the energy range of interest. These choices are appropriate for modeling moderately ionized, $\chi \gtrsim 0.01$, systems at $\sim$eV temperatures.

C. Multi-fluid simulations

The HiFi framework[13–15] uses the spectral element method with an implicit time advance to solve systems of partial differential equations written in conservative form. We use HiFi's plasma–neutral module[32] to perform 2D multi-fluid simulations of magnetic reconnection where the neutral and charged components are evolved separately. The system of multi-fluid equations are derived in Ref. 33. This model assumes quasineutrality in that the ion number density, n_i, equals the electron number density, n_e. Similarly, we assume that the ion pressure, p_i, equals the electron pressure, p_e. This module has been used to model reconnection in the solar chromosphere.[16–21]

The equations that are evolved by HiFi for the simulations in this paper have been modified from the equations solved by Refs. 16–21 to more closely match the physical effects included in the VPIC simulations and allow us to isolate the roles of kinetic effects. The simulations use the normalizations described in Sec. 2.1 of Ref. 18, except that the ion mass, m_i, is taken to be the mass of $^4_2\mathrm{He}^{1+}$ (i.e., 6.65×10^{-27} kg). In this section, we follow Refs. 16–18, 32 and 33 and summarize the multi-fluid model evolved by HiFi.

The ion and neutral continuity equations evolved by HiFi are

$$\frac{\partial n_i}{\partial t} + \nabla\cdot(n_i\mathbf{v}_i) = 0, \tag{11}$$

$$\frac{\partial n_n}{\partial t} + \nabla\cdot(n_n\mathbf{v}_n) = 0, \tag{12}$$

where n_i and n_n are the ion and neutral number densities, and $\mathbf{v}_i$ and $\mathbf{v}_n$ are the ion and neutral velocities. Strict quasineutrality is assumed such that $n_i \equiv n_e$, where n_e is the electron number density.

We assume an Ohm's law of the form

$$\mathbf{E} + \mathbf{v}_i\times\mathbf{B} = \eta\mathbf{J} + \frac{\mathbf{J}\times\mathbf{B}}{en_e} - \frac{\nabla p_e}{en_e} - \frac{m_e\nu_e}{en_e}\nabla^2\mathbf{J}, \tag{13}$$

where $\mathbf{E}$ is the electric field, $\mathbf{v}_i$ is the ion velocity, $\mathbf{B}$ is the magnetic field, η is the resistivity, $\mathbf{J}$ is the current density, p_e is the electron pressure, ν_e is the electron viscosity, m_e is the mass of an electron, and e is the elementary charge. While recent simulations with HiFi's plasma–-neutral module have included resistivity due to both electron–ion and electron–neutral collisions calculated as functions of local plasma parameters;[17,18] here, a constant and uniform resistivity that approximates the expected resistivity in the VPIC simulations is used instead.

The magnetic field is decomposed into the form

$$\mathbf{B} = \nabla\times\left(A_y\hat{\mathbf{y}}\right) + B_y\hat{\mathbf{y}}, \tag{14}$$

where A_y is the magnetic flux and B_y is the out-of-plane magnetic field. The evolution of A_y governs the evolution of B_x and B_z and is given by

$$\frac{\partial A_y}{\partial t} = -E_y. \tag{15}$$

By applying Eq. (13), Eq. (15) becomes

$$-\frac{\partial A_y}{\partial t} + \nabla\cdot\left(\frac{m_e\nu_e}{n_ee}\nabla\mathbf{J}\right) = -V_zB_x + V_xB_z + \eta J_y + \frac{J_xB_z - J_zB_x}{en_e}. \tag{16}$$

Similarly, the evolution of B_y is found by evaluating

$$\frac{\partial B_y}{\partial t} + \nabla\cdot(\mathbf{E}\times\hat{\mathbf{y}}) = 0. \tag{17}$$

The ion and neutral momentum equations are

$$\frac{\partial}{\partial t}(m_in_i\mathbf{v}_i) + \nabla\cdot(m_in_i\mathbf{v}_i\mathbf{v}_i + \mathsf{P}_i + \mathsf{P}_e) = \mathbf{J}\times\mathbf{B} + \mathbf{R}_i^{in} + \Gamma^{cx}m_i(\mathbf{v}_n - \mathbf{v}_i) + \mathbf{R}_{in}^{cx} - \mathbf{R}_{ni}^{cx}, \tag{18}$$

$$\frac{\partial}{\partial t}(m_in_n\mathbf{v}_n) + \nabla\cdot(m_in_n\mathbf{v}_n\mathbf{v}_n + \mathsf{P}_n) = -\mathbf{R}_i^{in} + \Gamma^{cx}m_i(\mathbf{v}_i - \mathbf{v}_n) - \mathbf{R}_{in}^{cx} + \mathbf{R}_{ni}^{cx}. \tag{19}$$

Momentum transfer due to identity-preserving collisions between ions and neutrals is given by

$$\mathbf{R}_i^{in} = m_{in} n_i \nu_{in} (\mathbf{v}_n - \mathbf{v}_i). \tag{20}$$

The reduced mass for collisions between particles of arbitrary species α and β is $m_{\alpha\beta} = m_\alpha m_\beta/(m_\alpha + m_\beta)$. The frequency for a particle of species α to collide with a particle of species β is given by

$$\nu_{\alpha\beta} = n_\beta \Sigma_{\alpha\beta} \sqrt{\frac{8 k_B T_{\alpha\beta}}{\pi m_{\alpha\beta}}}, \tag{21}$$

where $\Sigma_{\alpha\beta} = \Sigma_{\beta\alpha}$ is the collisional cross section, $T_{\alpha\beta} \equiv (m_\beta T_\alpha + m_\alpha T_\beta)/(m_\alpha + m_\beta)$, and k_B is the Boltzmann constant. For collisions between ${}_2^4\mathrm{He}^{0+}$ and ${}_2^4\mathrm{He}^{1+}$, a cross section of $\Sigma_{in} = 4 \times 10^{-19}$ m^2 is used.

The charge exchange reaction rate is

$$\Gamma^{cx} = \Sigma_{cx} n_i n_n v_{cx}. \tag{22}$$

The representative speed of charge exchange reactions is

$$v_{cx} \equiv \sqrt{\frac{4}{\pi} v_{Ti}^2 + \frac{4}{\pi} v_{Tn}^2 + v_{in}^2}. \tag{23}$$

The most probable thermal speed of species α is given by $v_{T\alpha} = \sqrt{2 k_B T_\alpha/m_\alpha}$. The cross section for charge exchange reactions between neutral and singly ionized helium is approximated as

$$\Sigma_{cx} = 6.64 \times 10^{-19} - 4.48 \times 10^{-20} \ln v_{cx}\,\mathrm{m}^2, \tag{24}$$

where v_{cx} is in units of m s^{-1}. The terms $\mathbf{R}_{in}^{cx}$ and $\mathbf{R}_{ni}^{cx}$ represent frictional forces due to charge exchange reactions and are given by[33]

$$\mathbf{R}_{in}^{cx} = -\frac{m_i \Sigma_{cx} n_i n_n v_{Tn}^2}{\sqrt{4\left(\frac{4}{\pi} v_{Ti}^2 + v_{in}^2\right) + \frac{9\pi}{4} v_{Tn}^2}} \mathbf{V}_{in}, \tag{25}$$

$$\mathbf{R}_{ni}^{cx} = \frac{m_i \Sigma_{cx} n_i n_n v_{Ti}^2}{\sqrt{4\left(\frac{4}{\pi} v_{Tn}^2 + v_{in}^2\right) + \frac{9\pi}{4} v_{Ti}^2}} \mathbf{V}_{in}. \tag{26}$$

The pressure tensor for species α is given by

$$\mathsf{P}_\alpha = p_\alpha \mathsf{I} + \pi_\alpha, \tag{27}$$

where p_α is the isotropic pressure and I is the identity dyadic tensor. The viscous stress tensor for species α is

$$\pi_\alpha = -\xi_\alpha \left[\nabla \mathbf{v}_\alpha + (\nabla \mathbf{v}_\alpha)^\top\right], \tag{28}$$

where ξ_α is the viscosity coefficient. Note that Eq. (28) does not include the $\nabla \cdot \mathbf{v}_\alpha$ term;[11] however, this is consistent with previously published results using HiFi.[16–21] The ion and neutral viscosity coefficients ξ_i and $\xi_n = 5.1 \times 10^{-5}$ kg m^{-1} s^{-1} are uniform.

The plasma–neutral module of HiFi evolves the plasma pressure, $p_p \equiv p_i + p_e$, and the neutral pressure, p_n. Plasma pressure evolution is given by[32]

$$\begin{aligned}\frac{1}{\gamma - 1}\frac{\partial p_p}{\partial t} + \nabla \cdot \left(\frac{\gamma}{\gamma - 1} p_p \mathbf{v}_i + \mathbf{v}_i \cdot \pi_p + \mathbf{h}_i + \mathbf{h}_e\right) \\ = \mathbf{v}_i \cdot \left[\nabla \cdot (p_p \mathsf{I} + \pi_p)\right] + \mathbf{J} \cdot \mathbf{E} - \mathbf{v}_i \cdot (\mathbf{J} \times \mathbf{B}) \\ + Q_i^{in} + Q_e^{en} + \mathbf{R}_{in}^{cx} \cdot (\mathbf{v}_n - \mathbf{v}_i) \\ + \frac{\Gamma^{cx} m_i}{2} (\mathbf{v}_i - \mathbf{v}_n)^2 + Q_{in}^{cx} - Q_{ni}^{cx}\end{aligned} \tag{29}$$

with $\pi_p \equiv \pi_i + \pi_e$. Neutral pressure evolution is given by[32]

$$\begin{aligned}\frac{1}{\gamma - 1}\frac{\partial p_n}{\partial t} + \nabla \cdot \left(\frac{\gamma}{\gamma - 1} p_n \mathbf{v}_n + \mathbf{v}_n \cdot \pi_n + \mathbf{h}_n\right) \\ = \mathbf{v}_n \cdot \left[\nabla \cdot (p_n \mathsf{I} + \pi_n)\right] + Q_i^{in} + Q_n^{en} \\ + \frac{1}{2}\Gamma^{cx} m_i (\mathbf{v}_i - \mathbf{v}_n)^2 + \mathbf{R}_{ni}^{cx} \cdot (\mathbf{v}_i - \mathbf{v}_n) + Q_{ni}^{cx} - Q_{in}^{cx}.\end{aligned} \tag{30}$$

The heat fluxes for the magnetized components $\alpha \in \{e, i\}$ are given by

$$\mathbf{h}_\alpha = \left[\kappa_{||,\alpha} \hat{\mathbf{b}}\hat{\mathbf{b}} + \kappa_{\perp,\alpha}(\mathsf{I} - \hat{\mathbf{b}}\hat{\mathbf{b}})\right] \cdot \nabla k_B T_\alpha, \tag{31}$$

where the coefficients $\kappa_{\perp,\alpha}$ and $\kappa_{||,\alpha}$ correspond to thermal conduction perpendicular and parallel to the magnetic field direction $\hat{\mathbf{b}}$, respectively. The values for $\kappa_{\perp,\alpha}$ and $\kappa_{||,\alpha}$ are calculated from Ref. 11. Neutral thermal conduction is isotropic and is given by

$$\mathbf{h}_n = -\kappa_n \nabla k_B T_n. \tag{32}$$

The heating of species α resulting from interactions with species β is given by[33]

$$Q_\alpha^{\alpha\beta} = \frac{1}{2}\mathbf{R}_\alpha^{\alpha\beta} \cdot (\mathbf{v}_\beta - \mathbf{v}_\alpha) + 3 m_{\alpha\beta} n_\alpha \nu_{\alpha\beta} (T_\beta - T_\alpha). \tag{33}$$

The terms $Q_{\alpha\beta}^{cx}$ correspond to heat transfer to species α from species β due to charge exchange reactions.[32–34]

The energy equations includes contributions from ion–neutral friction, charge exchange, Ohmic heating, viscous heating, and thermal energy transfer between species. The energy equation for the plasma includes anisotropic thermal conduction and Ohmic heating. The energy equation for neutrals includes isotropic thermal conduction. The energy equations evolved using HiFi for this paper do not include terms related to ionization, recombination, or optically thin radiative losses.

III. COMPARISON BETWEEN PIC AND MULTI-FLUID SIMULATIONS OF RECONNECTION

A. Simulation results

Using the methodologies described above, detailed comparisons between PIC and multi-fluid simulations of magnetic reconnection are performed. The PIC simulations presented have been previously described in Jara-Almonte *et al.*[22] and parameters and initial conditions for the multi-fluid simulations have been chosen to closely match this previous study. In addition to a well-matched set of cases, it is instructive to have a set of well-understood reference cases in the collisional regime against which Hall and kinetic effects can be compared. To that end, an additional set of multi-fluid simulations was performed where the resistivity was increased by a factor of approximately 2.35. This choice is somewhat arbitrary but, as discussed in Sec. III B,

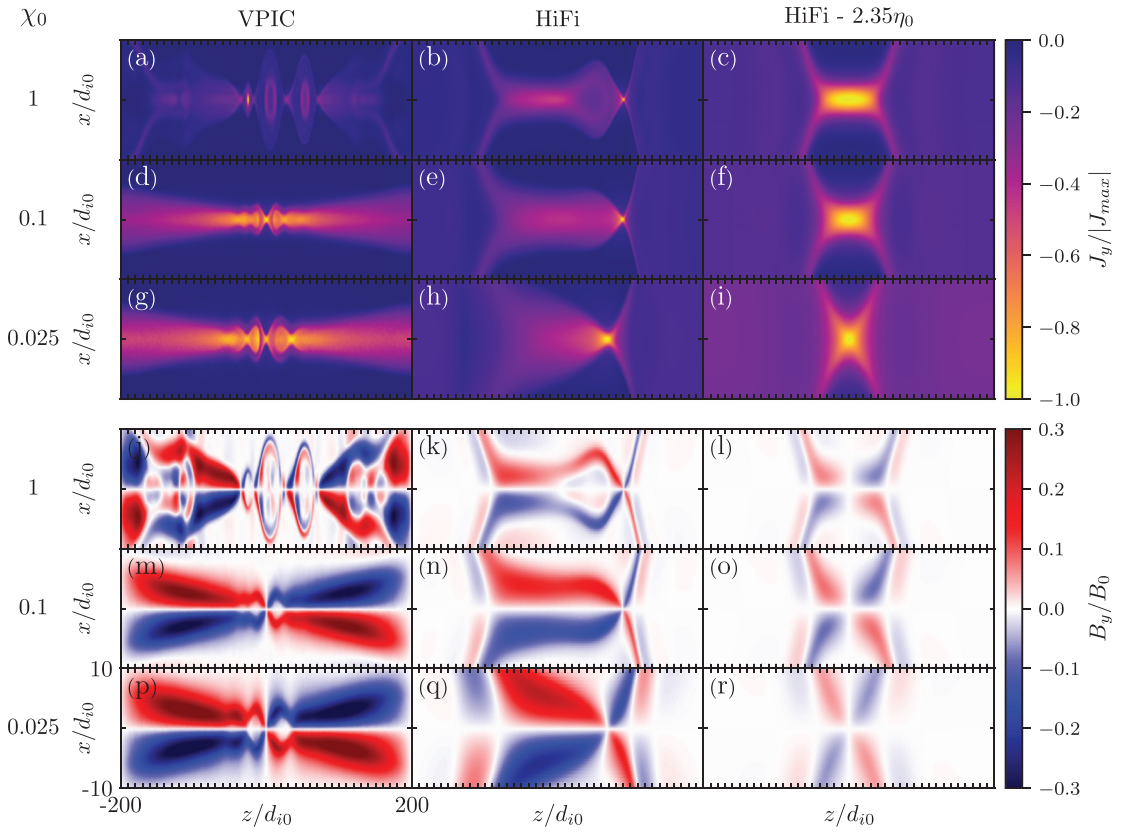

FIG. 2. Current sheet morphology for the different models tested and for initial ionization fractions $\chi_0 = 1$ [(a)–(c), (j)–(l)], 0.1 [(d)–(f), (m)–(o)], and 0.025 [(g)–(i), (p)–(r)]. Times shown are selected to be near the maximum reconnection rate. In all cases the simulation domain spans $\pm 100 d_{i0}$, in x and $\pm 200 d_{i0}$ in z, but only the inner $\pm 10 d_{i0}$ extent in x is shown here to highlight the current sheet structure. Ticks are uniformly drawn every $10 d_{i0}$ in both x and z. [(a)–(i)] The out-of-plane current density, J_y, normalized to its maximal value, $|J_{max}|$. [(j)–(r)] The out-of-plane magnetic field, B_y, normalized to the asymptotic reconnecting field, B_0. See text for discussion.

it ensures that $d_i < \delta < d^*$ which changes the reconnection regime. Within this set of simulations, only Sweet–Parker current sheets are formed.

In Fig. 2, the internal current sheet structure is shown; for example, cases at $\chi_0 = 1$, 0.1, and 0.025 and near the time of peak reconnection rate. Significant qualitative differences can be seen between the various models. In the fully ionized regime, $\chi_0 = 1$, the most apparent difference is that the Sweet–Parker current sheet in PIC simulations becomes unstable to the plasmoid instability whereas the multi-fluid simulations do not. This is due to the fact that the Coulomb collision operator in PIC self-consistently captures the $T_e^{-3/2}$ dependence of the collision frequency, which leads to runaway heating in the current sheet and an increase in the Lundquist number.[28] Within closed PIC simulations, this effect prevents a long-time study of the resistive regime.[35] That is why, only the multi-fluid model is used for benchmarking the resistive regime in this work.

Although previous HiFi studies have included this $T^{-3/2}$ dependence,[17] the assumption that $p_e = p_i = p_p/2$ is violated in fully ionized PIC simulations where $T_i \approx 2T_e$ within the current sheet; a more complete fluid model would be required to model this effect. In this manuscript, however, the emphasis is on the partially ionized regime. In this limit, ion–neutral charge exchange rapidly equilibrates the local ion and neutral temperatures, and the large thermal mass of neutrals prevents significant heating.[22] As a result, PIC simulations in the partially ionized regime have electrons that are only slightly hotter than ions, $T_e \approx$ (1–1.2) T_i, and the assumption that $p_e = p_i$ is a good approximation.

As shown in Figs. 2(d) and 2(g), it is typical for the reconnection current sheet in PIC simulations of partially ionized reconnection to have significant internal structure that is not captured in the corresponding multi-fluid simulations. It is common for small-scale magnetic islands to form, and these are hypothesized to be related to ion flow recirculation near the X-point during fast reconnection.[22] With the exception of these outflow islands, PIC simulations rapidly collapse down to a central X-point. In contrast, when well-matched multi-fluid simulations are performed, secondary tearing in the central current sheet leads to the formation of a single magnetic island in the center of the domain. To limit the effects of this, additional random density fluctuations are included in the initial conditions for the multi-fluid cases. These fluctuations explicitly break the symmetry in z and allow a single X-line to form. However, secondary tearing still plays an important role and the primary X-line is shifted far from the domain center.

The reconnection rate in all cases was measured and shown as a function of time for the $L_z = 400 d_{i0}$ cases in Fig. 3. A major difference

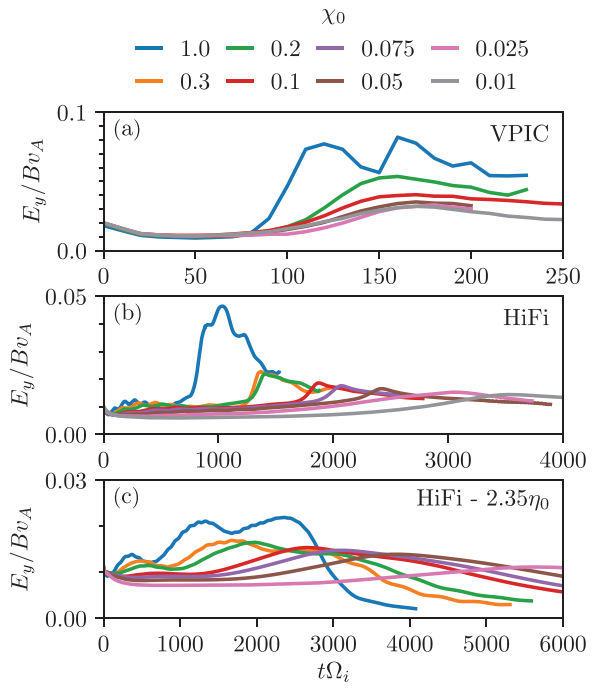

FIG. 3. Reconnection rate as a function of time for cases with $L_z = 400d_{i0}$. (a) PIC simulation results. (b). Matched multifluid simulation results. (c) Results from multi-fluid simulations with increased resistivity. See text for discussion.

between the different models is the timescale required in order for the reconnection rate to be maximized; in PIC this occurs within $\lesssim 200\Omega_i^{-1}$ ($800\Omega_i^{-1}$ for the $L_z = 800d_{i0}$, $\delta_0 = 2d_{i0}$ case, not shown), while multi-fluid simulations require several thousand Ω_i^{-1}. This discrepancy is directly related to the differences in initial current sheet thickness, see Sec. II A. It was found that when multi-fluid simulations were initialized with a thin current sheet, $\delta_0 = d_i$, as in PIC, Ohmic heating within the current sheet led to a rapid increase in the current sheet thickness which reduced the peak reconnection rate. By initializing the multi-fluid simulations with an initially thick current sheet and allowing it to self-consistently thin down, this effect can be mitigated. Although this is a major difference between the models tested, as discussed in Sec. II A, a PIC case with $\delta_0 = 2d_{i0}$ was performed to test the influence of initial thickness on the PIC results and little difference was found.

In addition to a difference in time scales, the reconnection rate achieved also differs significantly between models. In order to probe the physics underlying this difference, the time of peak reconnection rate is selected from each case for further analysis, and the peak rate is shown as a function of the upstream ionization fraction in Fig. 4(a). As has been previously reported, kinetic simulations obey a $\chi^{1/2}$ scaling at moderate ionization fraction, but become dependent on system size at low χ possibly due to boundary effects.[22] In contrast, the reconnection rate in both sets of multi-fluid simulations is both smaller than kinetic simulations and has a weaker ionization fraction dependence.

In order to understand the reconnection rate scalings in the multi-fluid simulations, it is instructive to recall the two fluid limits of partially ionized reconnection:[36] decoupled ions and neutrals, and fully coupled ions and neutrals. In the decoupled limit, neutrals play no role and the classical Sweet–Parker solution is obtained where the reconnection rate, $R \equiv E_y/Bv_A$, depends on the local Lundquist number, $S_{CS} \equiv \mu_0 L v_A/\eta$, as $R \approx S_{CS}^{-1/2}$, and the current sheet thickness is given by $\delta \approx L S_{CS}^{-1/2}$. Here, L and δ are the measured half-length and half-thickness of the current sheet. In the fully coupled limit, the ion Alfvén speed, $v_A = B/\sqrt{\mu_0 m_i n_i}$ is replaced with the bulk Alfvén speed $v_A^\star = v_A \chi^{1/2}$ (here, the superscript $\star$ refers to quantities that should be evaluated with the total mass, $m_i n_i + m_n n_n$, rather than the ion mass $m_i n_i$). Subsequently, the Sweet–Parker solution is modified as $R \approx \chi^{1/4} S_{CS}^{-1/2}$ and $\delta \approx \delta_{SP}^\star = L\chi^{-1/4} S_{CS}^{-1/2}$.

The current sheet width and length were measured as the half-width at half-max of the out-of-plane current density, J_y, along the inflow and outflow directions. Using the measured density and temperature (for the kinetic cases) at the X-line, the current sheet Lundquist number S_{CS} was computed, and in Fig. 4(b), the measured reconnection rate is compared with the decoupled Sweet–Parker rate. For the matched multi-fluid simulations, a constant value of ≈0.3 is obtained suggesting that the reconnection rate is constrained by decoupled Sweet–Parker physics. In generalized Sweet–Parker models, the scaling constant can differ from unity due to, e.g., effects from

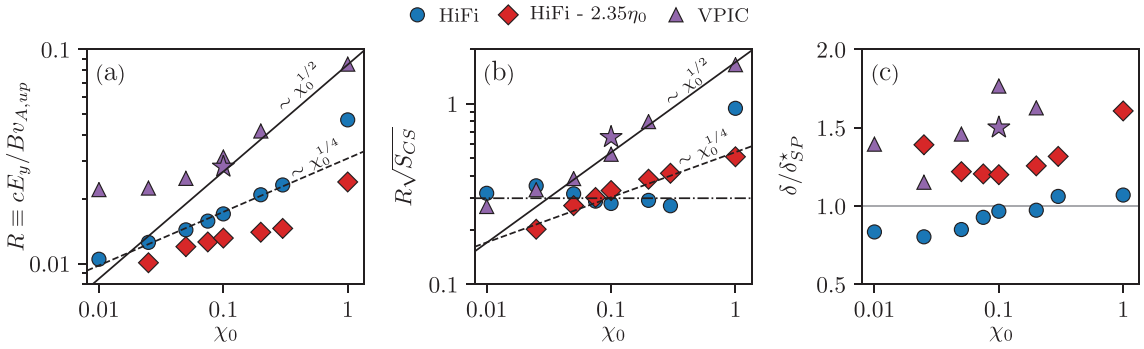

FIG. 4. Comparison between HiFi fluid simulations and VPIC particle-in-cell simulations of partially ionized magnetic reconnection. (a) The maximum reconnection rate, $R \equiv E_y/Bv_{A,up}$ (b) The reconnection rate normalized to the decoupled Sweet–Parker rate, $1/\sqrt{S_{CS}}$. (c) The current sheet thickness normalized to the fully coupled Sweet–Parker thickness, $\delta_{SP}^\star \equiv L\chi^{-1/4} S_{CS}^{-1/2}$. The fully ionized kinetic case ($\chi_0 = 1$, $\delta/\delta_{SP}^\star = 3.5$) is not shown for clarity. In all figures, the purple star denotes the VPIC case with $L_z = 800d_{i0}$, $\delta_0 = 2d_{i0}$.

compressibility and pressure gradients,[37] or outflow asymmetry.[38] In contrast, for the resistive multi-fluid simulations, a $\chi^{1/4}$ scaling is obtained, as expected of a fully-coupled Sweet–Parker model. Finally, the kinetic simulations show the same $\chi^{1/2}$ dependence since, as discussed below, L (and thus S_{CS}) does not significantly change with ionization fraction. These different scalings suggest that the physics controlling the reconnection rate is fundamentally different in each set of simulation.

In addition to the reconnection rate itself, Sweet–Parker models also predict the current sheet aspect ratio or equivalently the current sheet thickness when given L. In Fig. 4(c), the current sheet thickness normalized to the *fully coupled* Sweet–Parker thickness, $\delta^\star_{SP}$, is shown as a function of ionization fraction. With the exception of the fully ionized kinetic case, all simulations satisfy $\delta \approx \delta^\star_{SP}$ within a factor of two. This suggests that the current sheet structure is determined by fully coupled physics, despite the different physics underlying the reconnection rate. While this is an empirical observation, the underlying physics is not well understood. In particular, the current sheets in the kinetic simulations are sufficiently small scale such that ion and neutral outflows are locally decoupled at low χ, and thus it is not clear why $\delta^\star_{SP}$ is still a relevant length scale.

Although $\delta \approx \delta^\star_{SP}$ holds approximately across all cases, the manner in which this is achieved differs significantly. Figure 5 demonstrates how the scaling of δ and L differs in each set. In kinetic simulations, δ and L are relatively insensitive to ionization fraction, suggesting that the current sheet structure is primarily determined by local physics. Conversely, in the matched multi-fluid simulations, the current sheet thickness is found to scale with $d_0^\star \equiv d_{i0}\chi^{-1/2}$. Maintaining $\delta \sim d_0^\star \sim \delta^\star_{SP}$ requires that the current sheet length increase at low ionization fraction. If compressibility effects are neglected, then this would imply $L \sim d_0^\star$ as well, and the current sheet would be self-similar across χ_0. Instead, the scaling $L \sim d_{i0}\chi_0^{-3/4}$ is observed in the multi-fluid simulations. This additional factor can be accounted for by taking into account local changes in the ion and neutral density (i.e., $\chi \neq \chi_0$ and $n_i \neq n_{i0}$), and noting that the relation $\delta \approx \delta^\star_{SP}$ is based on *local* parameters, while $d_0^\star$ is evaluated using the initial Harris sheet density.

The scaling $\delta \sim d_0^\star$ is interesting because it was previously predicted by Malyshkin and Zweibel[24] who argued that this expansion of the current sheet would be balanced by a corresponding decrease in the outflow velocity and lead to an ionization fraction independent reconnection rate. To test this, the peak ion outflow velocity was measured in all simulations and shown in Fig. 5(c). In all models, the outflow velocity decreases with the ionization fractions, and for the matched multi-fluid simulations, the scaling is consistent with within 30% with the predicted $\chi_0^{1/2}$ decrease. However, the prediction of a constant reconnection rate strictly follows only under an assumption that L itself is ionization fraction independent (e.g., set by kinetic physics in the Hall regime). This is clearly not the case in the multi-fluid simulations. In these simulations, density variations partially compensate for the increased current sheet length, and the reconnection rate scales as $\chi_0^{1/4}$, see Fig. 4(a).

B. Physical regimes

As described above, the various sets of simulations show distinctly different behavior and scalings for the reconnection rate and current sheet structure. The reason that scalings are different is a direct result of distinct changes in the collisional and reconnection regimes for each set of simulations. Six different physical regimes for partially ionized reconnection have been identified based on two physical parameters: the effective collisionality, $\tilde{\nu}$, and the ratio of the Sweet–Parker width to the bulk inertial length, $\delta^\star_{SP}/d^\star$.[24] In the model of Malyshkin and Zweibel,[24] the effective collisionality is approximated by the solution to [Eq. (60) therein]

$$\tilde{\nu} \approx \frac{\nu_{ni} L}{v_A^\star} \min\left\{1, \sqrt{\chi(\tilde{\nu}+1)}\right\}. \tag{34}$$

For $\tilde{\nu} \ll \frac{\chi}{1-\chi}$, the Alfvén transit time through the current sheet is faster than ν_{in}^{-1} and neutrals are fully decoupled. Conversely, for $\tilde{\nu} \gg 1$ the Alfvén transit time is slower than ν_{ni}^{-1} and neutrals and ions are fully coupled throughout the outflow. In the intermediate regime, $\frac{\chi}{1-\chi} \ll \tilde{\nu} \ll 1$, multi-fluid effects and dissipation by ion–neutral friction are important.

Although Eq. (34) and the regimes identified are the result of a lengthy derivation, it may also be heuristically estimated from the well-known Kulsrud–Pearce dispersion relation for shear Alfvén waves in a partially ionized plasma.[39] For $\chi \ll 1$, shear Alfvén waves are cutoff in the intermediate (multi-fluid) region $2\chi^{1/2} < \nu_{ni}/k_\parallel v_A^\star < 1/2$. Wavenumbers below (above) the cutoff region correspond to fully coupled (fully decoupled) regimes. Up to factors of 2, the regimes

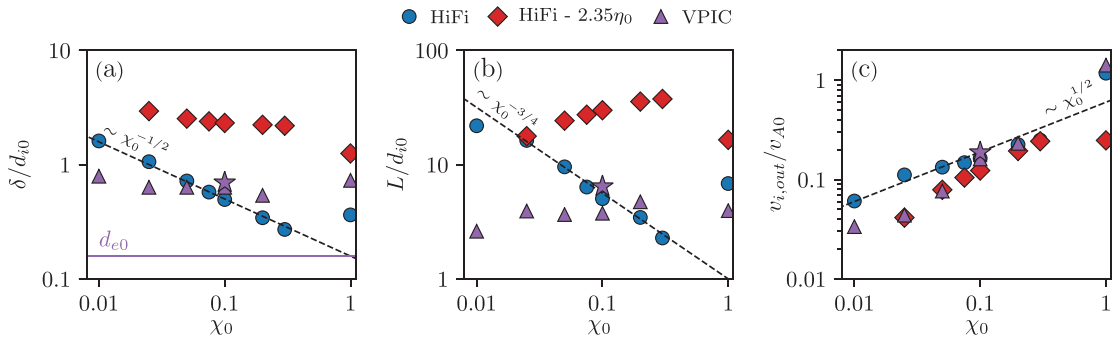

FIG. 5. Dependence of the (a) current sheet half-width δ, (b) half-length L and (c) peak ion outflow velocity on the upstream ionization fraction, χ_0. Dashed lines show reference scaling laws (not fits), and the lower purple line in (a) shows the value of the initial electron inertial length, d_{e0} in kinetic simulations. See text for discussion.

identified by Malyshkin and Zweibel[24] are equivalent to these cutoffs when setting $k_{\|} = L^{-1}$.

Finally, the two reconnection regimes identified are the resistive and Hall regimes. The boundary between the two was suggested to occur at $\delta^{\star}_{SP}/d^{\star} = 1$ based on an extrapolation of fully ionized reconnection physics,[24] but previously it has been shown that in simulations the boundary does not occur at $\delta^{\star}_{SP}/d^{\star} = 1$ but instead at $\delta/d_i \approx 1$.[19,22]

The parameters $\nu_{ni}L/v^{\star}_A$ and $\delta^{\star}_{SP}/d^{\star}$ have been evaluated for all simulation cases and are shown relative to the predicted regime boundaries in Fig. 6(a). For all HiFi cases, and nearly all VPIC cases, $1 < \sqrt{\chi(\tilde{\nu}+1)}$ such that $\tilde{\nu} \approx \nu_{ni}L/v^{\star}_A$. As seen in previous studies, even the resistive cases fall well below the $\delta^{\star}_{SP}/d^{\star} = 1$ boundary and all cases would be expected to undergo Hall reconnection. As demonstrated above, the resistive cases follow a fully coupled Sweet–Parker scaling, and thus are categorized incorrectly by Fig. 6(a). Note that the existence of the quadrupolar structure in the out-of-plane magnetic field, a result of the Hall effect, in Figs. 2(l), 2(o), and 2(r) does not necessarily contradict being in the resistive regime. Previous results have shown that the Hall fields remain even in resistive regime, albeit at reduced magnitudes.[26,40] By modifying the boundary to $\delta^{\star}_{SP}/d_i = 1$, the resistive cases are lifted into the fully-coupled resistive regime. After this modification, the matched multi-fluid simulations fall into a transition region between $1 \lesssim \nu_{ni}L/v^{\star}_A \lesssim 2$,that is roughly aligned with the predicted boundary at $\nu_{ni}L/v^{\star}_A = 1$, Fig. 6(b).

It is significant that, while the multi-fluid simulations appear to maintain $\nu_{ni}L/v^{\star}_A \gtrsim 1$, the current sheet length in PIC simulations is insensitive to χ and $\nu_{in}L/v_A \sim 2-4$ always (not shown). In this study, since $\lambda_{in}/d_i = 0.5$ and $\beta_{i,up} = 0.15$ are held constant, it cannot be determined whether the current sheet length in PIC simulations is set by kinetic (i.e., d_i) or collisional (i.e., v_A/ν_{in}) processes. If the length is controlled by the latter, however, then one possible explanation for the difference between the kinetic and multi-fluid simulations is in a fundamental difference in how fast reconnection is initiated.

In the case of a slow, global collapse of a fully-coupled Sweet–Parker current sheet, one might expect the long wavelength Alfvén cutoff, $\nu_{ni}L/v^{\star}_A \approx 1$, to play an important role in preventing the current sheet collapse to small scales. On the other hand, if reconnection is initiated by a localized perturbation, then one might expect the short wavelength Alfvén cutoff, $\nu_{in}L/v_A \approx 1$, to play an important role in preventing the perturbation from growing to large scales. Thus, these results are nominally consistent with a hypothesis that fast reconnection starts at global scales in multi-fluid simulations, but is instead locally triggered in kinetic simulations. Future well-controlled studies (e.g., fixed χ, variable λ_{in}/d_i) are required to definitively test these ideas.

The idea that $\nu_{in}L/v_A \approx 1$ plays an important role in setting the current sheet length at small scales is also consistent with previous experimental results.[23] The approximate boundaries of that study are shown in Fig. 6(b), where $\delta \approx \delta^{\star}_{SP}$ is assumed for the experimental data. In the experiments, the electron temperature was higher than in this study, $T_{e,\,\mathrm{exp}} \approx 6$ eV, and electron neutral collisions are only negligible for $\chi \gtrsim 0.03$ (based on an electron–neutral momentum exchange cross section of $\approx 6 \times 10^{-20}$ m^2). When this condition is satisfied, experimental data satisfy $\nu_{in}L/v_A \approx 1-3$, although for $\chi \lesssim 0.03$, $\nu_{in}L/v_A$ is larger.

IV. CONCLUSIONS

Here, multi-fluid and kinetic models of partially ionized magnetic reconnection have been directly compared for the first time. The different models are shown to have systematic differences in both the current sheet structure and scaling of the reconnection rate. As has been previously shown, kinetic simulations[22] and laboratory experiments[23] have demonstrated a reconnection rate scaling of $\chi^{1/2}$, i.e., $E_y \sim Bv^{\star}_A$. Conversely, the reconnection rate in multi-fluid simulations obeys either a fully coupled or a decoupled Sweet–Parker scaling depending on the resistivity. In both cases, the reconnection rate is smaller than in kinetic simulations and laboratory experiments. Interestingly, the local current sheet appears to obey the scaling relation $\delta \sim \delta^{\star}_{SP}$ in all cases. This implies that even on small scales where there is significant decoupling between ion and neutral flows, neutral physics plays an important role in determining the current sheet structure. This suggests that even a weak frictional coupling between ions and a (static) neutral background could modify the current sheet structure, and is an interesting topic for future study.

To understand these results, it was argued the multi-fluid simulations operate in different physical regimes from the kinetic simulations and experiments. In multi-fluid simulations, the current sheet length appears limited by a constraint that $\nu_{ni}L/v^{\star}_A \gtrsim 1$, which is violated in both kinetic simulations and experiments. One possible explanation is

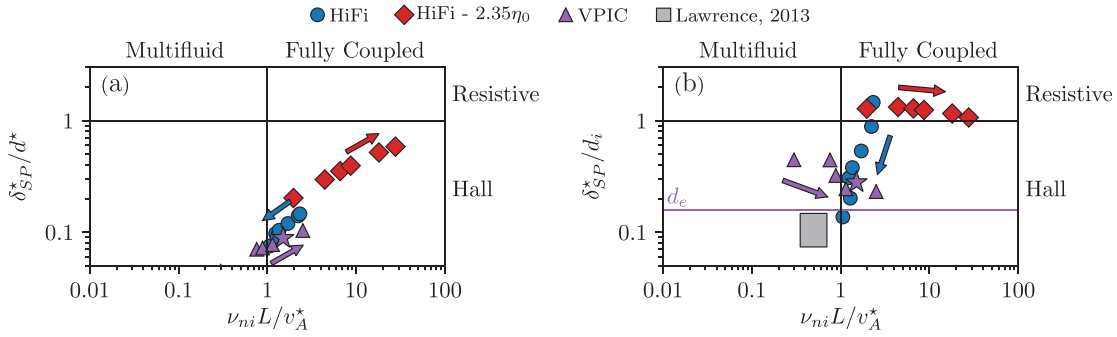

FIG. 6. Simulation results relative to some of the regimes of partially ionized reconnection. (a) Regimes identified using the parameters suggested in Malyshkin and Zweibel.[24] (b) Modification of the reconnection parameter from $\delta^{\star}_{SP}/d^{\star}$ to $\delta^{\star}_{SP}/d_i$ more clearly organizes the data. Boundaries of the experimental data from Lawrence *et al.*[23] are shown as well. Colored arrows show the direction of increasing χ, while the purple horizontal line in (b) shows the $\delta^{\star}_{SP}/d_e = 1$ boundary in the kinetic simulations (for experimental data, $d_e/d_i = 0.012$). Fully ionized cases are not shown.

that the mechanism by which Hall reconnection is triggered, either globally or locally, differs in the two models. If this is the case, then, in the partially ionized limit, the reconnection "rate" and "onset" problems may not be cleanly separated as they are in the fully ionized case. In particular, the problem of when and how the onset of reconnection happens remains a major open question even in fully ionized plasmas.[41] Understanding when and how fast reconnection can occur has significant implications for reconnection in the solar chromosphere, interstellar medium, molecular clouds, and other partially ionized systems.[4,10]

ACKNOWLEDGMENTS

The authors thank W. S. Daughton for helpful discussion and V. S. Lukin, E. T. Meier, J. Leake, and L. Ni for code development on HiFi and its plasma–neutral module and past simulation efforts that made this work possible. This research was supported by NASA Grant No. H-TIDES NNH15AB29I, with corresponding subcontract S014981-F from Princeton University to the Smithsonian Astrophysical Observatory (SAO). J.J-A. acknowledges partial support by Max Planck Princeton Center for Plasma Physics (MPPC) funded by DoE through Contract No. DE-AC0209CH11466. N.A.M. acknowledges partial support from NSF Grant No. 1931388, NASA Grant Nos. 80NSSC18K1124 and 80NSSC20K0174, and NASA Contract No. NNM07AB07C to SAO. This research made use of PlasmaPy version 0.3.1,[42] an open source Python package for plasma physics developed with support from NSF, DoE, and NASA. The multi-fluid simulations performed for this paper were conducted on the Smithsonian Institution High Performance Cluster.[43] This research has made use of NASA's Astrophysics Data System Bibliographic Services.

Some kinetic simulations were performed on computational resources managed and supported by Princeton Research Computing, a consortium of groups including the Princeton Institute for Computational Science and Engineering (PICSciE) and the Office of Information Technology's High Performance Computing Center and Visualization Laboratory at Princeton University. An award of computer time was also provided by the Innovative and Novel Computational Impact on Theory and Experiment (INCITE) program. This research used resources of the Argonne Leadership Computing Facility, which is a DoE Office of Science User Facility supported under Contract No. DE-AC02–06CH11357.

DATA AVAILABILITY

The data that support the findings of this study are openly available in the Princeton University DataSpace, Ref. 44.

REFERENCES

[1]E. G. Zweibel and M. Yamada, "Magnetic reconnection in astrophysical and laboratory plasmas," Annu. Rev. Astron. Astrophys. **47**, 291–332 (2009).
[2]M. Yamada, R. Kulsrud, and H. Ji, "Magnetic reconnection," Rev. Mod. Phys. **82**, 603–664 (2010).
[3]W. Gonzalez and E. Parker, *Magnetic Reconnection* (Springer, 2016), Vol. 427.
[4]L. Ni, H. Ji, N. A. Murphy, and J. Jara-Almonte, "Magnetic reconnection in partially ionized plasmas," Proc. R. Soc. A **476**, 20190867 (2020).
[5]K. Shibata, T. Nakamura, T. Matsumoto, K. Otsuji, T. J. Okamoto, N. Nishizuka, T. Kawate, H. Watanabe, S. Nagata, S. UeNo, R. Kitai, S. Nozawa, S. Tsuneta, Y. Suematsu, K. Ichimoto, T. Shimizu, Y. Katsukawa, T. D. Tarbell, T. E. Berger, B. W. Lites, R. A. Shine, and A. M. Title, "Chromospheric anemone jets as evidence of ubiquitous reconnection," Science **318**, 1591 (2007).
[6]H. Tian, E. E. DeLuca, S. R. Cranmer, B. De Pontieu, H. Peter, J. Martínez-Sykora, L. Golub, S. McKillop, K. K. Reeves, M. P. Miralles, P. McCauley, S. Saar, P. Testa, M. Weber, N. Murphy, J. Lemen, A. Title, P. Boerner, N. Hurlburt, T. D. Tarbell, J. P. Wuelser, L. Kleint, C. Kankelborg, S. Jaeggli, M. Carlsson, V. Hansteen, and S. W. McIntosh, "Prevalence of small-scale jets from the networks of the solar transition region and chromosphere," Science **346**, 1255711 (2014).
[7]F. Ellerman, "Solar hydrogen 'bombs'," Astrophys. J. **46**, 298 (1917).
[8]H. Tian, Z. Xu, J. He, and C. Madsen, "Are IRIS bombs connected to Ellerman bombs?," Astrophys. J. **824**, 96 (2016).
[9]H. Peter, H. Tian, W. Curdt, D. Schmit, D. Innes, B. De Pontieu, J. Lemen, A. Title, P. Boerner, N. Hurlburt, T. D. Tarbell, J. P. Wuelser, J. Martínez-Sykora, L. Kleint, L. Golub, S. McKillop, K. K. Reeves, S. Saar, P. Testa, C. Kankelborg, S. Jaeggli, M. Carlsson, and V. Hansteen, "Hot explosions in the cool atmosphere of the Sun," Science **346**, 1255726 (2014).
[10]H. Ji and W. Daughton, "Phase diagram for magnetic reconnection in heliophysical, astrophysical, and laboratory plasmas," Phys. Plasmas **18**, 111207 (2011).
[11]S. I. Braginskii, "Transport processes in a plasma," Rev. Plasma Phys. **1**, 205 (1965).
[12]A. Brandenburg and E. G. Zweibel, "The formation of sharp structures by ambipolar diffusion," Astrophys. J. Lett. **427**, L91 (1994).
[13]V. S. Lukin, A. H. Glasser, W. Lowrie, and E. T. Meier, "Overview of HiFi—Implicit spectral element code framework for multi-fluid plasma applications," arXiv:1608.06030 (2016).
[14]V. S. Lukin, "Computational study of the internal kink mode evolution and associated magnetic reconnection phenomena," Ph.D. thesis (Princeton University, 2008).
[15]A. H. Glasser and X. Z. Tang, "The SEL macroscopic modeling code," Comput. Phys. Commun. **164**, 237–243 (2004).
[16]J. E. Leake, V. S. Lukin, M. G. Linton, and E. T. Meier, "Multi-fluid simulations of chromospheric magnetic reconnection in a weakly ionized reacting plasma," Astrophys. J. **760**, 109 (2012).
[17]J. E. Leake, V. S. Lukin, and M. G. Linton, "Magnetic reconnection in a weakly ionized plasma," Phys. Plasmas **20**, 061202 (2013).
[18]N. A. Murphy and V. S. Lukin, "Asymmetric magnetic reconnection in weakly ionized chromospheric plasmas," Astrophys. J. **805**, 134 (2015).
[19]L. Ni, V. S. Lukin, N. A. Murphy, and J. Lin, "Magnetic reconnection in strongly magnetized regions of the low solar chromosphere," Astrophys. J. **852**, 95 (2018).
[20]L. Ni, V. S. Lukin, N. A. Murphy, and J. Lin, "Magnetic reconnection in the low solar chromosphere with a more realistic radiative cooling model," Phys. Plasmas **25**, 042903 (2018).
[21]L. Ni and V. S. Lukin, "Onset of secondary instabilities and plasma heating during magnetic reconnection in strongly magnetized regions of the low solar atmosphere," Astrophys. J. **868**, 144 (2018).
[22]J. Jara-Almonte, H. Ji, J. Yoo, M. Yamada, W. Fox, and W. Daughton, "Kinetic simulations of magnetic reconnection in partially ionized plasmas," Phys. Rev. Lett. **122**, 015101 (2019).
[23]E. E. Lawrence, H. Ji, M. Yamada, and J. Yoo, "Laboratory study of hall reconnection in partially ionized plasmas," Phys. Rev. Lett. **110**, 015001 (2013).
[24]L. M. Malyshkin and E. G. Zweibel, "Onset of fast magnetic reconnection in partially ionized gases," Astrophys. J. **739**, 72 (2011).
[25]K. J. Bowers, B. J. Albright, L. Yin, B. Bergen, and T. J. T. Kwan, "Ultrahigh performance three-dimensional electromagnetic relativistic kinetic plasma simulation," Phys. Plasmas **15**, 055703 (2008).
[26]W. Daughton, V. Roytershteyn, B. J. Albright, H. Karimabadi, L. Yin, and K. J. Bowers, "Influence of Coulomb collisions on the structure of reconnection layers," Phys. Plasmas **16**, 072117 (2009).
[27]V. Roytershteyn, W. Daughton, S. Dorfman, Y. Ren, H. Ji, M. Yamada, H. Karimabadi, L. Yin, B. Albright, and K. Bowers, "Driven magnetic reconnection near the Dreicer limit," Phys. Plasmas **17**, 055706 (2010).

[28]A. Stanier, W. Daughton, A. Le, X. Li, and R. Bird, "Influence of 3d plasmoid dynamics on the transition from collisional to kinetic reconnection," Phys. Plasmas **26**, 072121 (2019).
[29]T. Takizuka and H. Abe, "A binary collision model for plasma simulation with a particle code," J. Comput. Phys. **25**, 205–219 (1977).
[30]C. K. Birdsall, "Particle-in-cell charged-particle simulations, plus monte carlo collisions with neutral atoms, pic-mcc," IEEE Trans. Plasma Sci. **19**, 65–85 (1991).
[31]R. W. Schunk, "Mathematical structure of transport equations for multispecies flows," Rev. Geophys. **15**, 429–445, https://doi.org/10.1029/RG015i004p00429 (1977).
[32]E. T. Meier, "Modeling plasmas with strong anisotropy, neutral fluid effects, and open boundaries," Ph.D. thesis (University of Washington, 2011).
[33]E. T. Meier and U. Shumlak, "A general nonlinear fluid model for reacting plasma-neutral mixtures," Phys. Plasmas **19**, 072508 (2012).
[34]H. L. Pauls, G. P. Zank, and L. L. Williams, "Interaction of the solar wind with the local interstellar medium," J. Geophys. Res. **100**, 21595–21604, https://doi.org/10.1029/95JA02023 (1995).
[35]J. Jara-Almonte and H. Ji, "A thermodynamic phase transition during magnetic reconnection," Phys. Rev. Lett. (submitted).
[36]E. G. Zweibel, "Magnetic reconnection in partially ionized gases," Astrophys. J. **340**, 550 (1989).
[37]H. Ji, M. Yamada, S. Hsu, and R. Kulsrud, "Experimental test of the sweet-parker model of magnetic reconnection," Phys. Rev. Lett. **80**, 3256–3259 (1998).
[38]N. A. Murphy, C. Sovinec, and P. Cassak, "Magnetic reconnection with asymmetry in the outflow direction," J. Geophys. Res.: Space Phys. **115**, A9; (2010).
[39]R. Kulsrud and W. P. Pearce, "The effect of wave-particle interactions on the propagation of cosmic rays," Astrophys. J. **156**, 445 (1969).
[40]Y. Ren, M. Yamada, S. Gerhardt, H. Ji, R. Kulsrud, and A. Kuritsyn, "Experimental verification of the hall effect during magnetic reconnection in a laboratory plasma," Phys. Rev. Lett. **95**, 055003 (2005).
[41]H. Ji, J. Karpen, A. Alt, S. Antiochos, S. Baalrud, S. Bale, P. M. Bellan, M. Begelman, A. Beresnyak, A. Bhattacharjee, E. G. Blackman, D. Brennan, M. Brown, J. Buechner, J. Burch, P. Cassak, B. Chen, L. J. Chen, Y. Chen, A. Chien, L. Comisso, D. Craig, J. Dahlin, W. Daughton, E. DeLuca, C. F. Dong, S. Dorfman, J. Drake, F. Ebrahimi, J. Egedal, R. Ergun, G. Eyink, Y. Fan, G. Fiksel, C. Forest, W. Fox, D. Froula, K. Fujimoto, L. Gao, K. Genestreti, S. Gibson, M. Goldstein, F. Guo, J. Hare, M. Hesse, M. Hoshino, Q. Hu, Y. M. Huang, J. Jara-Almonte, H. Karimabadi, J. Klimchuk, M. Kunz, K. Kusano, A. Lazarian, A. Le, S. Lebedev, H. Li, X. Li, Y. Lin, M. Linton, Y. H. Liu, W. Liu, D. Longcope, N. Loureiro, Q. M. Lu, Z.-W. Ma, W. H. Matthaeus, D. Meyerhofer, F. Mozer, T. Munsat, N. A. Murphy, P. Nilson, Y. Ono, M. Opher, H. Park, S. Parker, M. Petropoulou, T. Phan, S. Prager, M. Rempel, C. Ren, Y. Ren, R. Rosner, V. Roytershteyn, J. Sarff, A. Savcheva, D. Schaffner, K. Schoeffler, E. Scime, M. Shay, L. Sironi, M. Sitnov, A. Stanier, M. Swisdak, J. TenBarge, T. Tharp, D. Uzdensky, A. Vaivads, M. Velli, E. Vishniac, H. Wang, G. Werner, C. Xiao, M. Yamada, T. Yokoyama, J. Yoo, S. Zenitani, and E. Zweibel, "Major scientific challenges and opportunities in understanding magnetic reconnection and related explosive phenomena in solar and heliospheric plasmas," e-print arXiv:2009.08779 (2020).
[42]PlasmaPy Community, D. Stańczak, E. Everson, N. A. Murphy, P. M. Kozlowski, R. Malhotra, S. J. Langendorf, A. J. Leonard, D. Stansby, C. C. Haggerty, S. J. Mumford, J. P. Beckers, M. S. Bedmutha, J. Bergeron, L. Bessi, S. Carroll, S. Chambers, A. Choubey, J. Deal, R. Díaz Pérez, L. Einhorn, T. Fan, S. I. Farid, G. Goudeau, S. Guidoni, R. S. Hansen, J. Hillairet, P. Z. How, Y.-M. Huang, N. Humphrey, M. Isupova, J. Kent, S. Kulshrestha, P. Kuszaj, P. L. Lim, A. Magarde, J. V. Martinelli, J. Munn, T. Parashar, N. Patel, J. Polak, A. Rao, R. Raj, A. Savcheva, C. Shen, D. N. Sherpa, F. Silva, A. Singh, A. Singh, B. Sipőcz, A. Tavant, T. Varnish, S. Xu, C. Zhang, and D. Diaz (2020). "PlasmaPy 0.3.1," Zenodo.
[43]Smithsonian Institution, "Smithsonian Institution High Performance Computing Cluster," see https://doi.org/10.25572/SIHPC.
[44]J. Jara-Almonte, N. Murphy, and H. Ji, "Multi-fluid and kinetic models of partially ionized magnetic reconnection" (Princeton University, 2021), see http://arks.princeton.edu/ark:/88435/dsp01sj1395028.